



HAL
open science

Analytic modeling of breakdown voltage shift in the CMOS buried multiple junction detector

Thais Luana Vidal de Negreiros da Silva, Pascal Kleimann, Patrick Pittet,
Guo-Neng Lu

► **To cite this version:**

Thais Luana Vidal de Negreiros da Silva, Pascal Kleimann, Patrick Pittet, Guo-Neng Lu. Analytic modeling of breakdown voltage shift in the CMOS buried multiple junction detector. *Solid-State Electronics*, 2020, 164, pp.107682. 10.1016/j.sse.2019.107682 . hal-02463250

HAL Id: hal-02463250

<https://univ-lyon1.hal.science/hal-02463250>

Submitted on 21 Dec 2021

HAL is a multi-disciplinary open access archive for the deposit and dissemination of scientific research documents, whether they are published or not. The documents may come from teaching and research institutions in France or abroad, or from public or private research centers.

L'archive ouverte pluridisciplinaire **HAL**, est destinée au dépôt et à la diffusion de documents scientifiques de niveau recherche, publiés ou non, émanant des établissements d'enseignement et de recherche français ou étrangers, des laboratoires publics ou privés.



Distributed under a Creative Commons Attribution - NonCommercial 4.0 International License

Analytic Modeling of Breakdown Voltage Shift in the CMOS Buried Multiple Junction Detector

Thais Luana Vidal de Negreiros da Silva^a, Pascal Kleimann^a, Patrick Pittet^{a*}, Guo-Neng Lu^a

^aLyon Institute of Nanotechnology, Université Claude Bernard Lyon 1, Université de Lyon
 Villeurbanne 69100, France

Abstract—We propose an analytical model for the CMOS Buried Multiple Junction (BMJ) detector exhibiting breakdown voltage shift depending on adjacent junction’s bias. The device’s singular behavior has been observed when two adjacent junctions are in reach-through (RT) condition. The breakdown current has been identified to be predominated by thermionic emission. The proposed model determines, for a given BMJ structure with uniform or Gaussian doping distributions under bias conditions, whether two adjacent junctions are in RT condition. In this case, it calculates the merged depletion limits, electric field and electrostatic potential profile. The potential barrier height of each merged depletion region can then be extracted and the thermionic current be computed.

Model computations have been compared with TCAD simulations and measurements on the BMJ detector. Good agreements have been observed for different structures in different bias conditions at different temperatures.

Keywords—analytical model, breakdown voltage shift, buried multiple junction (BMJ) detector, thermionic emission

I. INTRODUCTION

The Buried Multiple Junction (BMJ) detector consists of multiple vertically-stacked p-n junctions. The detector device with up to four stacked junctions has been implemented in CMOS process [1]–[3]. Fig. 1 shows the device structure of the four stacked junctions in CMOS, called Buried Quad Junction (BQJ) detector.

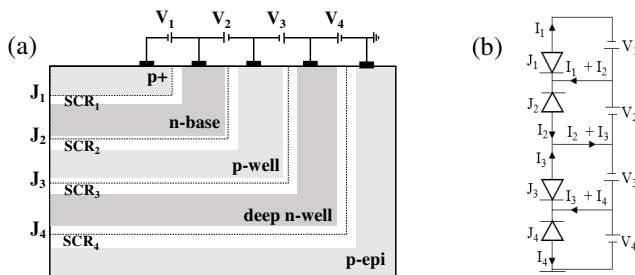


Fig. 1: Buried Quad Junction (BQJ) detector geometry (a) cross section and (b) electric equivalent circuit

These devices present the capability of spectral discrimination in the visible and near-infrared ranges [4],

* Corresponding author: patrick.pittet@univ-lyon1.fr

which have been explored as a color sensor in commercial cameras [5]. Most recently, they have been used for wavelength-sensitive analysis and weak signal detection, including multi-dye fluorescence application [6], pulse oximetry [7], as well as optical oxygen sensor [8].

The BMJ detector has typically been operated in photoconductive mode, with all junctions reverse biased below breakdown voltage. Some models have been proposed for BMJ detector in this mode of operation [9]. Moreover, the device behavior under high voltage bias has recently been investigated and a singular characteristic has been observed: The breakdown voltage of one buried junction may shift linearly with the bias voltage of its adjacent junction, as shown on Fig. 2 [10].

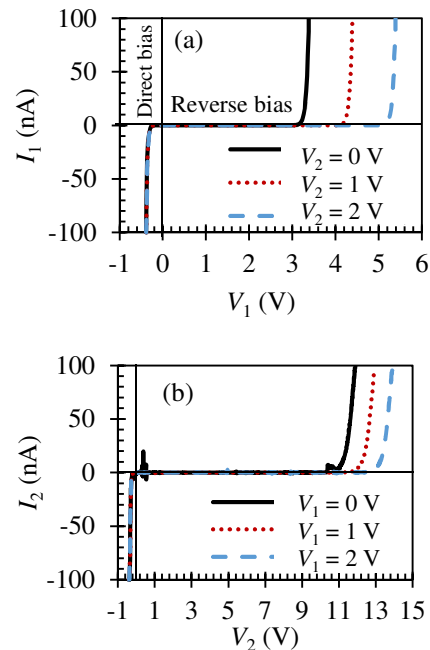


Fig. 2: I-V characteristics measured on a BQJ detector fabricated in Teledyne DALSA Semiconductor (Bromont, Canada) 0.8- μ m HV CMOS process (a) for the p+/n-base junction (J_1) and (b) for the p-well/n-base junction (J_2); p-well/deep-n-well and p-epi/deep-n-well are shortened ($V_3 = V_4 = 0$) [10].

In this paper, we propose to investigate into this singular behavior of the BMJ detector. By analyzing physical mechanisms inside the detector device, we have established an analytical model describing the breakdown mechanism of

buried junctions under high-voltage reverse bias. To validate our model, we have compared computed characteristics of the device from our model with Technology Computer-Aided Design (TCAD) simulations on the one hand, and with measured data on the other.

II. MODELING

A. Model description for uniform doping distributions

To describe our model, we consider the case of a BDJ detector – a *pnp* structure built with uniformly doped layers. Fig. 3 illustrates the detector structure in a reverse bias condition, with two reverse bias voltages V_k and V_{k+1} applied to J_k and J_{k+1} , respectively. In moderate reverse bias conditions, the depletion regions of J_k and J_{k+1} are separated by a Quasi-Neutral Region (QNR), as shown in Fig. 3a.

When increasing reverse bias voltages V_k and/or V_{k+1} , the QNR at the middle becomes narrow and finally disappears [8][9]. We call this as critical reach-through (RT) condition (see Fig. 3b). The corresponding reverse voltages are denoted as $V_{k,RT}$ and $V_{k+1,RT}$. As the two depletion regions in n-type layer merge, we have [13][14]:

$$W_{k,2} + W_{k+1,1} = x_{J_{k+1}} - x_{J_k} \quad (1)$$

where x_{J_k} and $x_{J_{k+1}}$ are the two junctions' depths, respectively.

For both cases of Fig. 3a and Fig. 3b, the depletion layer widths of the BDJ structure have the following relationships:

$$W_{k,1} = \sqrt{\frac{2\epsilon}{q} \frac{N_D}{N_{A,k}(N_D + N_{A,k})} (V_k + \psi_{bi,k})} \quad (2a)$$

$$W_{k,2} = \sqrt{\frac{2\epsilon}{q} \frac{N_{A,k}}{N_D(N_{A,k} + N_D)} (V_k + \psi_{bi,k})} \quad (2b)$$

$$W_{k+1,1} = \sqrt{\frac{2\epsilon}{q} \frac{N_{A,k+1}}{N_D(N_{A,k+1} + N_D)} (V_{k+1} + \psi_{bi,k+1})} \quad (2c)$$

$$W_{k+1,2} = \sqrt{\frac{2\epsilon}{q} \frac{N_D}{N_{A,k+1}(N_D + N_{A,k+1})} (V_{k+1} + \psi_{bi,k+1})} \quad (2d)$$

where $W_{k,1}$, $W_{k,2}$, $W_{k+1,1}$ and $W_{k+1,2}$ are the depletion widths

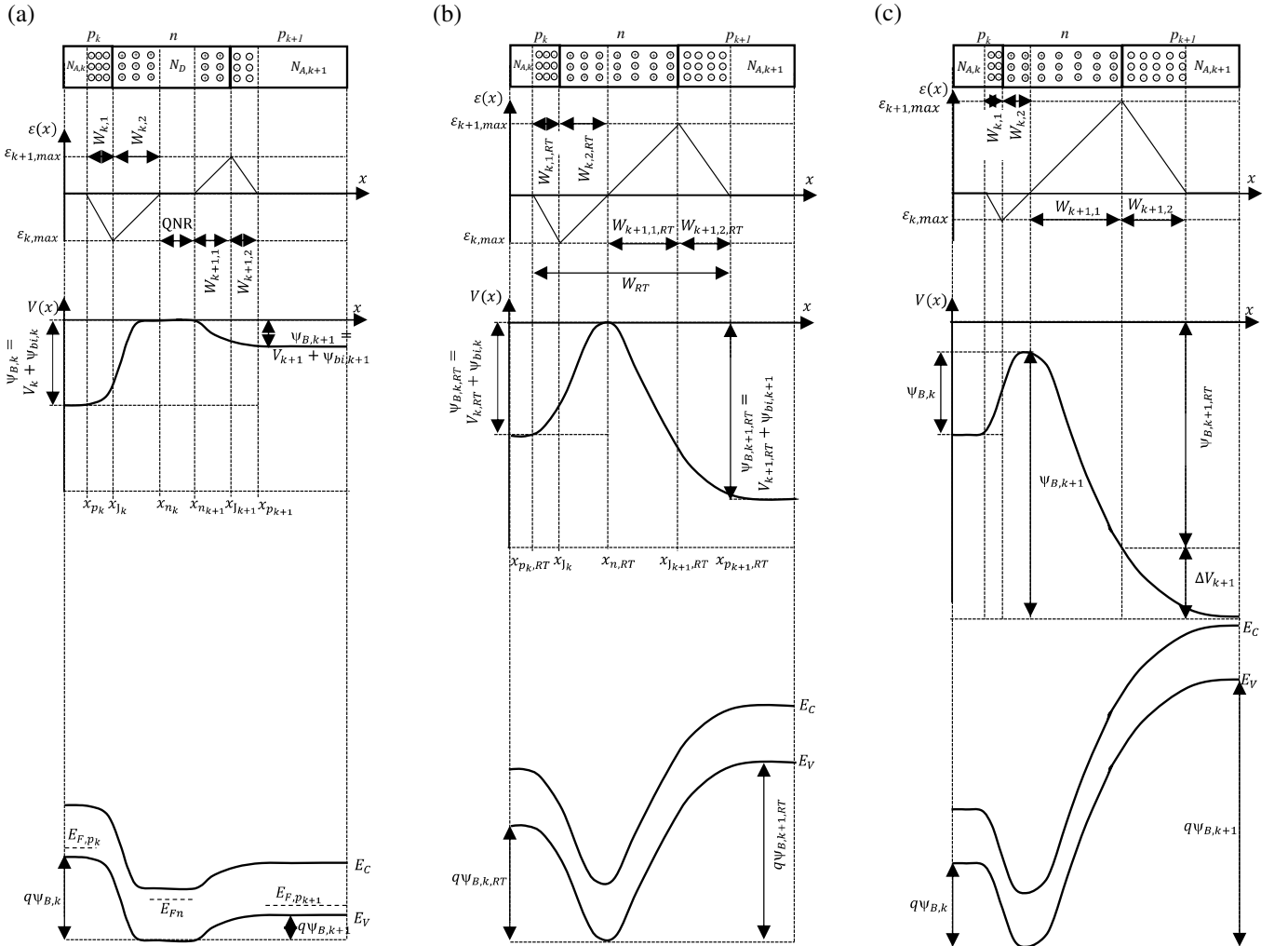


Fig. 3: Electric field $\epsilon(x)$, electrostatic potential $V(x)$ and conduction and valence energy bands, E_C and E_V , over a uniformly doped *pnp* structure in (a) low voltage bias condition; (b) critical RT condition; and (c) non-critical RT condition with $V_k = V_{k,RT}$ and $V_{k+1} > V_{k+1,RT}$.

in the p_k , n and p_{k+1} layers of J_k and J_{k+1} , respectively; $N_{A,k}$, N_D and $N_{A,k+1}$ are the acceptor and donor ionized impurity densities in p_k , n and p_{k+1} layers, respectively; $\psi_{bi,k}$ and $\psi_{bi,k+1}$ are the built-in voltage of J_k and J_{k+1} , respectively.

In critical RT condition (Fig. 3b), $V_{k+1,RT}$ is related to $V_{k,RT}$. This relationship can be established based on (1) combined with (2b) and (2c) and is given by:

$$V_{k+1,RT} = \frac{\left(x_{J_{k+1}} - x_{J_k} - \sqrt{\frac{2\epsilon}{q} \frac{N_{A,k}}{N_D(N_{A,k} + N_D)} (V_{k,RT} + \psi_{bi,k})} \right)^2}{\frac{2\epsilon}{q} \frac{N_{A,k+1}}{N_D(N_{A,k+1} + N_D)}} - \psi_{bi,k+1} \quad (3)$$

When further increasing on V_k and/or V_{k+1} (i.e. $V_k \geq V_{k,RT}$ and/or $V_{k+1} \geq V_{k+1,RT}$), the BDJ structure is biased in RT conditions as shown in Fig. 4. Most particularly, Fig. 3c illustrate such a condition, with $V_k = V_{k,RT}$ and $V_{k+1} > V_{k+1,RT}$. It is noted that RT biasing conditions were also observed for BARITT devices [13][14], as well as for punch-through diodes [15][16] and bulk-barrier diodes [17]. However

n layer having reached its maximum. This results in the following relationship:

$$N_{A,k}W_{k,1} + N_{A,k+1}W_{k+1,2} = N_D(x_{J_{k+1}} - x_{J_k}) \quad (5)$$

The electrostatic potential is obtained by integrating (4):

$$V(x) = \begin{cases} \frac{qN_{A,k}}{2\epsilon}(x - x_{J_k} + W_{k,1})^2 - (V_k + \psi_{bi,k}), & \text{for } x \in [x_{J_k} - W_{k,1}; x_{J_k}] \\ -\frac{qN_D}{2\epsilon}(x - x_{J_k} - W_{k,1} \frac{N_{A,k}}{N_D})^2 + \frac{q}{2\epsilon N_D}(N_{A,k}^2 + N_{A,k}N_D)W_{k,1}^2 - (V_k + \psi_{bi,k}), & \text{for } x \in [x_{J_k}; x_{J_{k+1}}] \\ \frac{qN_{A,k+1}}{2\epsilon}(x - x_{J_{k+1}} - W_{k+1,2})^2 - (V_{k+1} + \psi_{bi,k+1}), & \text{for } x \in [x_{J_{k+1}}; x_{J_{k+1}} + W_{k+1,2}] \end{cases} \quad (6)$$

The continuity of the electrostatic potential at $x_{J_{k+1}}$ gives a second relationship between $W_{k,1}$ and $W_{k+1,2}$, i.e.:

$$N_{A,k+1}W_{k+1,2}^2 + \frac{[(x_{J_{k+1}} - x_{J_k})N_D - W_{k,1}N_{A,k}]^2}{N_D} - \frac{N_{A,k}}{N_D}(N_{A,k} + N_D)W_{k,1}^2 = \frac{2\epsilon}{q}[(V_{k+1} - V_k) + (\psi_{bi,k+1} - \psi_{bi,k})] \quad (7)$$

Thus, $W_{k,1}$ and $W_{k+1,2}$ can be determined according to the

$$W_{k,1} = \frac{N_{A,k}(N_{A,k+1} + N_D)(x_{J_{k+1}} - x_{J_k}) - \sqrt{N_{A,k}N_{A,k+1}(x_{J_{k+1}} - x_{J_k})^2(N_{A,k+1} + N_D)(N_{A,k} + N_D) + \frac{2\epsilon}{q}[(V_{k+1} - V_k) + (\psi_{bi,k+1} - \psi_{bi,k})]N_{A,k}N_{A,k+1}(N_{A,k} - N_{A,k+1})}}{N_{A,k}(N_{A,k} - N_{A,k+1})} \quad (8a)$$

$$W_{k+1,2} = \frac{N_D}{N_{A,k+1}}(x_{J_{k+1}} - x_{J_k}) - \frac{N_{A,k}}{N_{A,k+1}} \frac{N_{A,k}(N_{A,k+1} + N_D)(x_{J_{k+1}} - x_{J_k}) - \sqrt{N_{A,k}N_{A,k+1}(x_{J_{k+1}} - x_{J_k})^2(N_{A,k+1} + N_D)(N_{A,k} + N_D) + \frac{2\epsilon}{q}[(V_{k+1} - V_k) + (\psi_{bi,k+1} - \psi_{bi,k})]N_{A,k}N_{A,k+1}(N_{A,k} - N_{A,k+1})}}{N_{A,k}(N_{A,k} - N_{A,k+1})} \quad (8b)$$

the biasing condition and/or structure were not comparable to BQJ detectors.

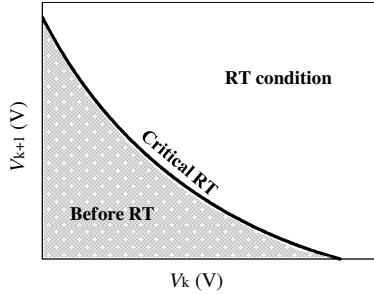


Fig. 4: RT biasing conditions.

In RT conditions, equation (1) still holds, and the electric field depends only of $W_{k,1}$ and $W_{k+1,2}$, since the distance between the junction is constant. The electric field in RT conditions (Fig. 3b and Fig. 3c) can be expressed as:

$$\epsilon(x) = \begin{cases} -\frac{qN_{A,k}}{\epsilon}(x - x_{J_k} + W_{k,1}), & \text{if } x \in [x_{J_k} - W_{k,1}; x_{J_k}] \\ \frac{qN_D}{\epsilon}(x - x_{J_k} - W_{k,1} \frac{N_{A,k}}{N_D}), & \text{if } x \in [x_{J_k}; x_{J_{k+1}}] \\ -\frac{qN_{A,k+1}}{\epsilon}(x - x_{J_{k+1}} - W_{k+1,2}), & \text{if } x \in [x_{J_{k+1}}; x_{J_{k+1}} + W_{k+1,2}] \end{cases} \quad (4)$$

It is worth mentioning that equations (2a)-(2d) are no longer valid in RT condition for determining the depletion widths. However, the total charge neutrality of the BDJ structure in RT conditions still holds, with a total charge in the

equations (5) and (7). They are expressed as:

The electrostatic potential reaches a maximum, V_{max} , at a position x_0 such as:

$$\left. \frac{dV(x)}{dx} \right|_{x=x_0} = 0 \quad (9)$$

The corresponding potential barrier for hole carriers can be determined as:

$$\psi_B = \begin{cases} \psi_{B_k}, & \text{if } V_{k+1} > V_k \\ \psi_{B_{k+1}}, & \text{if } V_{k+1} < V_k \end{cases} \quad (10)$$

where $\psi_{B_k} = V_{max} - V(x_{J_k} - W_{k,1})$ and $\psi_{B_{k+1}} = V_{max} - V(x_{J_{k+1}} + W_{k+1,2})$.

If $V_{k+1} > V_k$ (case illustrated in Fig. 3b and Fig. 3c), then $\psi_B = \psi_{B_k}$ and:

$$x_0 = x_{J_k} + W_{k,1} \frac{N_{A,k}}{N_D} \quad (11)$$

The maximum of the electrostatic potential can be expressed as:

$$V_{max} = V(x_0) = \frac{q}{2\epsilon N_D}(N_{A,k}^2 + N_{A,k}N_D)W_{k,1}^2 - (V_k + \psi_{bi,k}) \quad (12)$$

and the barrier height is thus given by:

$$\psi_B = \psi_{B_k} = \frac{q}{2\epsilon N_D} (N_{A,k}^2 + N_{A,k} N_D) W_{k,1}^2 \quad (13)$$

According to (8a) and (13), it appears that the barrier height does not depend independently of V_k and V_{k+1} , but only on their difference ($V_{k+1} - V_k$).

In RT condition, there is a thermionic current I_p flowing through the barrier across the BDJ structure, which is given by [18]:

$$I_p = i_0 T^2 e^{-\frac{q}{kT} \psi_B}, \quad (14)$$

where T the temperature, q is the elementary charge, k is the Boltzmann constant, and $i_0 = SA^*$, with A^* the Richardson constant for holes thermionic emission and S the active area of the detector.

When the barrier height is low enough, the thermionic current becomes predominant as compared to the other dark current components and the breakdown occurs. This current predominance can explain the breakdown voltage shift observed for the BDJ detectors [10]: the current level when breakdown occurs depends of the barrier height (ψ_B) which depends only on ($V_{k+1} - V_k$).

Thus, $V_{bd_{k+1}}(V_k)$, the breakdown voltage of J_{k+1} when J_k is biased by V_k , is related to $V_{bd_{k+1}}(0)$, the breakdown voltage when J_k is shortened, as follows:

$$V_{bd_{k+1}}(V_k) = V_{bd_{k+1}}(0) + V_k \quad (15)$$

B. Model adaptation for Gaussian doping distributions

BMJ structures fabricated in a CMOS process exhibit Gaussian doping profiles. For example, the BQJ structure presented in Fig. 1 (with four buried junctions) is obtained by one dopant diffusion (p_+ layer), three dopant implantations (nb , p_w and n_w layers) on a uniformly doped substrate (p_{sub}). The doping profile for this structure can be expressed as [19]:

$$N(x) = -N_{A,p+}(x) + N_{D,n}(x) - N_{A,pw}(x) + N_{D,nw}(x) - N_{A,psub}(x) \quad (16)$$

with:

$$N_{A,p+}(x) = N_{A,p+}(0) e^{-\frac{x^2}{\sigma_{p+}^2}} \quad (17a)$$

$$N_{D,nb}(x) = N_{D,nb}(0) e^{-\frac{x^2}{\sigma_{nb}^2}} \quad (17b)$$

$$N_{A,pw}(x) = N_{A,pw}(0) e^{-\frac{x^2}{\sigma_{pw}^2}} \quad (17c)$$

$$N_{D,nw}(x) = N_{D,nw}(0) e^{-\frac{x^2}{\sigma_{nw}^2}} \quad (17d)$$

and

$$N_{A,psub}(x) = N_{A,psub}(0) \quad (17e)$$

where $N_{A,p+}(0)$, $N_{D,nb}(0)$, $N_{A,pw}(0)$, $N_{D,nw}(0)$ and $N_{A,psub}(0)$ are the donor and acceptor concentrations at the surface of the BQJ structure. Typically $N_{A,p+}(0) > N_{D,nb}(0) > N_{A,pw}(0) > N_{D,nw}(0) > N_{A,psub}(0)$ and $\sigma_{p+} < \sigma_{nb} < \sigma_{pw} < \sigma_{nw}$.

The junction's depths in this structure are given by [19]:

$$x_{J_1} \approx \frac{\sigma_{p+} \sigma_{nb}}{\sqrt{\sigma_{nb}^2 - \sigma_{p+}^2}} \sqrt{\ln \left(\frac{N_{A,p+}(0)}{N_{D,nb}(0)} \right)}, \quad (18a)$$

$$x_{J_2} \approx \frac{\sigma_{nb} \sigma_{pw}}{\sqrt{\sigma_{pw}^2 - \sigma_{nb}^2}} \sqrt{\ln \left(\frac{N_{D,nb}(0)}{N_{A,pw}(0)} \right)}, \quad (18b)$$

$$x_{J_3} \approx \frac{\sigma_{pw} \sigma_{nw}}{\sqrt{\sigma_{nw}^2 - \sigma_{pw}^2}} \sqrt{\ln \left(\frac{N_{A,pw}(0)}{N_{D,nw}(0)} \right)} \quad (18c)$$

and

$$x_{J_4} \approx \frac{\sigma_{nw} \sigma_{psub}}{\sqrt{\sigma_{psub}^2 - \sigma_{nw}^2}} \sqrt{\ln \left(\frac{N_{D,nw}(0)}{N_{A,psub}(0)} \right)}. \quad (18d)$$

It is noted that, for each junction, the electric field reaches its maximum at the junction's depth x_{J_k} , i.e.:

$$\mathcal{E}_{k,max} = \frac{q}{\epsilon} \int_{x_{J_k} - W_{k,1}}^{x_{J_k}} N(u) du = \frac{q}{\epsilon} \int_{x_{J_k}}^{x_{J_k} + W_{k,2}} N(u) du \quad (19)$$

This establishes a relationship between the maximum electric field, $\mathcal{E}_{k,max}$, and the junction's depletion extensions, $W_{k,1}$ and $W_{k,2}$. (19) is an equation including two variables, $W_{k,1}$ and $W_{k,2}$. Both variables are functions of the applied voltage, V_k , to the considered junction J_k .

Consider now an adjacent junction J_{k+1} . Another equation including $W_{k+1,1}$ and $W_{k+1,2}$ is given by:

$$\mathcal{E}_{k+1,max} = \frac{q}{\epsilon} \int_{x_{J_{k+1}} - W_{k+1,1}}^{x_{J_{k+1}}} N(u) du = \frac{q}{\epsilon} \int_{x_{J_{k+1}}}^{x_{J_{k+1}} + W_{k+1,2}} N(u) du \quad (20)$$

Both $W_{k+1,1}$ and $W_{k+1,2}$ are functions of the applied voltage V_{k+1} to the considered junction J_{k+1} .

It is worth mentioning that equations (19) and (20) are no longer valid in RT condition (except for critical RT condition) for determining the depletion widths. However, the total charge neutrality of the BDJ structure in RT conditions still holds and gives the following relationship:

$$\int_{x_{J_k} - W_{k,1}}^{x_{J_k}} N(u) du + \int_{x_{J_{k+1}}}^{x_{J_{k+1}} + W_{k+1,2}} N(u) du = \int_{x_{J_k}}^{x_{J_{k+1}}} N(u) du \quad (21)$$

On the other hand, the electric field in the depletion region is given by:

$$\mathcal{E}(x) = \frac{q}{\epsilon} \int_{x_{J_k} - W_{k,1}}^x N(u) du \quad (22)$$

Integrating the electric field over the depletion region, we obtain a relationship between the depletion region limits and the junction's biasing voltages:

$$\int_{x_{J_k} - W_{k,1}}^{x_{J_{k+1}} + W_{k+1,2}} \mathcal{E}(u) du = (V_{k+1} - V_k) + (\psi_{bl,k+1} - \psi_{bl,k}) \quad (23)$$

It is worth mentioning that equations (21) and (23) correspond, respectively, to (5) and (7) for the uniformly doped case.

Solving the equations (21) and (23) determines the depletion limits of the two junctions in RT conditions $W_{k,1}$ and $W_{k+1,2}$. Once $W_{k,1}$ and $W_{k+1,2}$ are determined, the electrostatic potential of the two considered junctions in RT conditions, $V(x)$, is obtained by integrating the electric field, i.e.:

$$V(x) = - \int_{x|_k - W_{k,1}}^x \mathcal{E}(u) du \quad (24)$$

The potential barrier height of these two merged junctions and its position are then determined in the same way as that already described for the uniform doping distribution case.

C. Model implementation

The proposed model has been implemented using Matlab tool. It allows computations of breakdown current (due to thermionic emission) for a given BMJ structure with specific doping distributions. The model input parameters are the junctions' depth, the doping distributions and the biasing voltages.

For a set of bias voltages, the model firstly uses (1) to detect whether or not the buried junctions are in RT condition. Secondly, for the junctions in RT condition, each merged depletion region between two adjacent junctions is determined in terms of depletions limits, electric field and electrostatic potential profile by using (21), (22), (23) and (24). Thirdly, the potential barrier height of each merged depletion region is extracted according to (10). Finally, the corresponding thermionic current is computed by using (14).

III. MODEL VALIDATION AND DISCUSSIONS

A. BDJ *pnp* structure

To validate our proposed model, we consider first a BDJ (*pnp* structure), with uniform and Gaussian doping distributions, as shown in Fig. 5. It consists in comparing model computations with 2D TCAD simulations. The simulation software is from Sentaurus Workbench, Synopsys Inc. USA, with the following activated physical models for our studies: Masetti model for carrier mobility; SRH for generation/recombination process; van Overstraeten-de Man and Hurkx models for avalanche and band-to-band (BTB) mechanisms, respectively. Firstly, we verify the applied bias voltages corresponding to the critical RT condition. It amounts to verifying the depletion limits determined from the model.

For the BDJ structure in critical RT condition for a given bias voltage, e.g. $V_{1,RT}$, the model computations determine the other bias voltage $V_{2,RT}$. In TCAD simulations on the same structure, for a given $V_{1,RT}$, a sweep of the other bias voltage V_2 is applied to detect whether the two junctions' depletion regions merge. Fig. 6 shows the TCAD-simulated BDJ structure, before (Fig. 6a) and after (Fig. 6b) the merge between the two depletion regions. The depletion limits obtained by simulations are depicted by a white line, which

correspond to a drop to a 5 % of carrier concentration of the nearest QNR region.

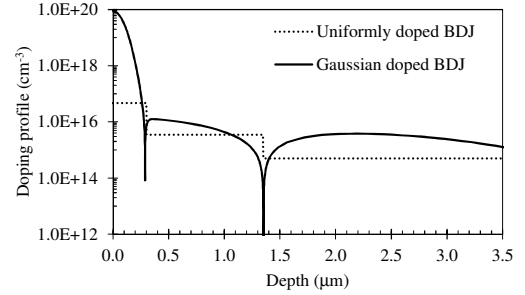


Fig. 5: Doping profile and junction's depths for uniformly and Gaussian doped BDJ detectors.

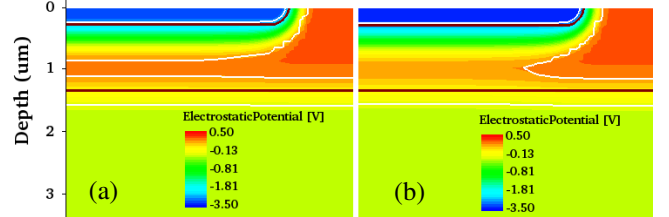


Fig. 6: Electrostatic potential simulated (a) before RT, for $V_1 = 2.5$ V and (b) after RT, for $V_1 = 2.7$ V ($V_2 = 0$ V on both cases).

Fig. 7 shows the required bias voltages to achieve RT conditions, obtained by the model computations and TCAD simulations, for both uniform and Gaussian doping distributions. It is noted that the critical RT condition exhibits a monolithic decrease: increasing $V_{1,RT}$ corresponds to a decreased $V_{2,RT}$. For both uniform and Gaussian doping cases, the obtained results show a good agreement, with a slight underestimation from the model. This may be due to the difference in defining depletion limits between the model and TCAD simulations.

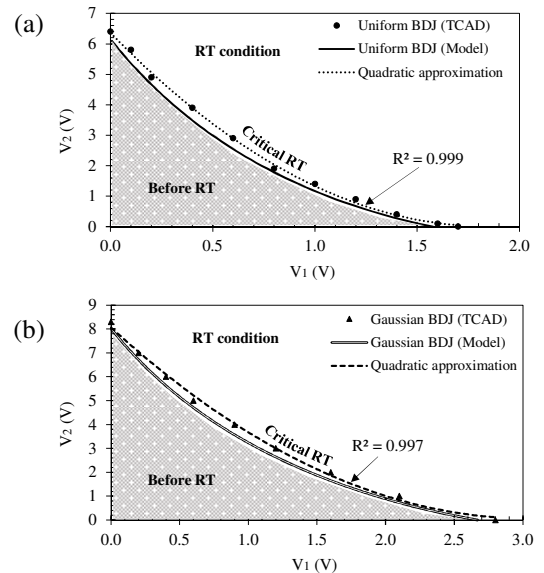


Fig. 7: Required V_1 and V_2 bias voltages to achieve RT conditions, obtained by the model computations and TCAD simulations obtained by TCAD simulation and by the model for a (a) uniform and (b) a Gaussian doping profiles at 300 K.

Furthermore, we verify the electrostatic potential across the BDJ structure in different bias conditions. Fig. 8 compares modeling results with TCAD-simulated ones for uniform (Fig. 8a) and Gaussian (Fig. 8b) doping distributions. The obtained results are in good agreement, with differences in $\Delta V(x)$ below 60 mV for different depths and bias conditions.

From the electrostatic potential of the BDJ structure in RT condition, corresponding to the applied bias voltages V_1 and V_2 , the potential barrier height can be extracted, as already presented by (9) and (10). From Fig. 8, we can see that the potential barrier height is in the first junction region for similar bias conditions. However, the barrier height is also modulated by the second junction's applied voltage, V_2 . Fig. 9 shows the dependence of the potential barrier height on V_2 for each given V_1 . For both uniform and Gaussian doping distributions, there is a good agreement between model and simulated results.

For the determined barrier height, the breakdown electric current across the barrier is determined by model. The temperature dependence of this current is compared with that from TCAD simulations. Fig. 10 plots the normalized breakdown current as a function of temperature (with breakdown current at 300 K as a reference). For different temperatures, the model computations are always in accordance with TCAD-simulated results.

B. BQJ structure

A BQJ detector (see Fig. 1) has been designed and fabricated in a 0.8- μm HV CMOS process (Teledyne DALSA). Its I-V characteristics in dark conditions have been determined. Both measured and TCAD simulated results on the BQJ structure can be compared with model calculations. The doping profiles of the structure used in the model and TCAD simulations are shown in Fig. 11. The diffusion and implanted layer are assumed to have Gaussian distributions, a part from the uniformly distributed substrate.

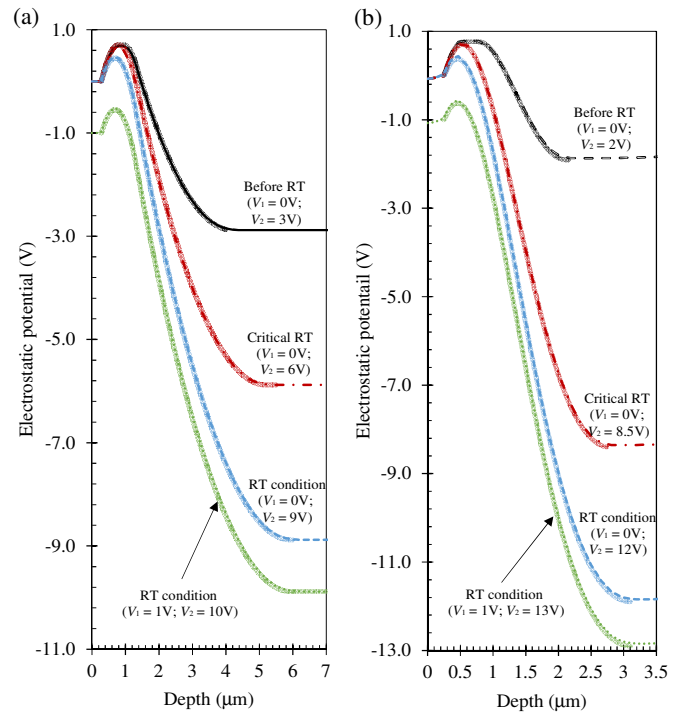


Fig. 8: 1D electrostatic potential obtained by TCAD simulation (dotted lines) and by the proposed model (continuous lines) for a (a) uniform and for a (b) Gaussian doping profile BDJ structure at 300 K.

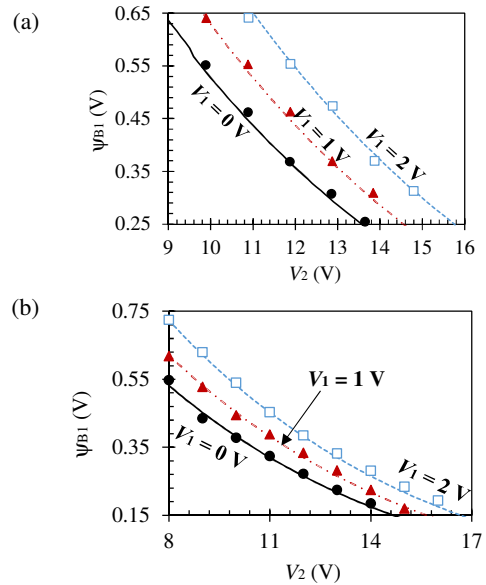


Fig. 9: Dependency of the potential barrier height ψ_{B1} with bias voltages V_1 and V_2 obtained by the proposed model (lines) and by TCAD simulations (dots) for (a) uniform and (b) Gaussian BDJ structure.

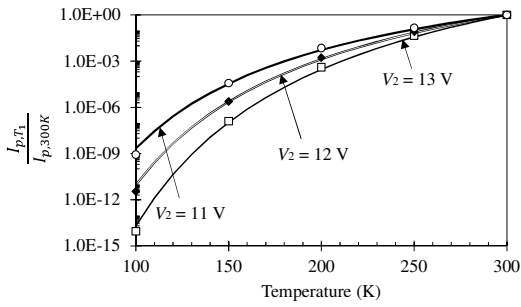


Fig. 10: Ratio between breakdown currents at different for the BQJ detector obtained by TCAD simulation (lines) and model (dots) for $V_1 = 0$ V.

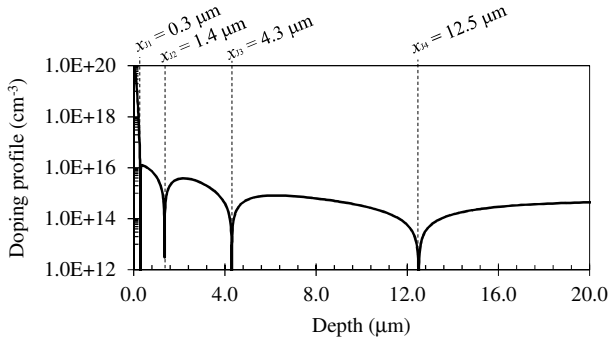


Fig. 11: Doping profile and junction's depths for a BQJ detector fabricated in a $0.8\text{-}\mu\text{m}$ HV CMOS process (Teledyne DALSA).

Fig. 12 shows I-V characteristics of the BQJ structure obtained from the model on the one hand and by simulations and measurements on the other.

Fig. 12a shows that the breakdown voltage of the first junction shifts with the bias voltage of the second junction. The breakdown voltage shifting predicted by the model exhibits a good accuracy. We can also observe a significant difference of the dark current before breakdown between TCAD simulations and measurements. This may be due to the fact that the dark current may be dominated by lateral surface thermal generation of the device, which has not been taken into account in TCAD simulations.

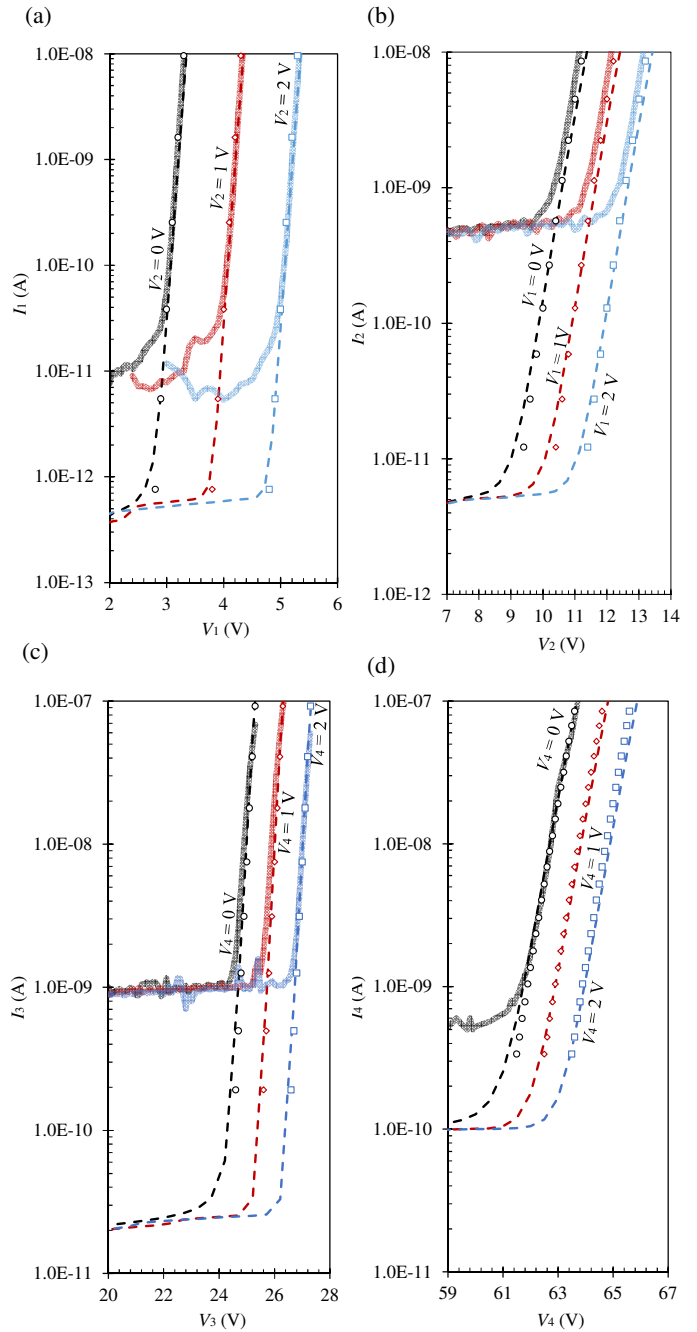


Fig. 12: I-V characteristics of the BQJ detector (at 300 K), showing breakdown that depends on adjacent junction's bias voltage: (a) for J_1 ; (b) for J_2 ; (c) for J_3 ; (d) and for J_4 , respectively. Comparison between model calculations (dots), TCAD simulations (dashed lines) and measurements (thick lines).

Fig. 12b presents the breakdown voltage shifting of the second junction depending on the first junction's bias voltage. For the breakdown voltage shifting, there is a good consistency between model prediction and TCAD simulations. However, a deviation of 0.3 V is observed when compared with measurements. This may be attributed to the assumed doping distributions (shown in Fig. 11), that does not correspond exactly to the fabricated device. For the dark current before breakdown, the differences between simulations and measurements are still larger than that of the first junction. This

seems to confirm that the lateral thermal generation is predominant, in particular for the relatively light-doped second junction. Fig. 12c and 12d corresponds to the case of J_3 and J_4 , respectively, showing similar results.

The breakdown voltage shift depending on the adjacent junction's bias voltage is plotted in Fig. 13. The plotted breakdown voltage corresponds to a given breakdown current at 1 nA. This dependency is linear, as can be seen from (15). The obtained simulated and measured results have confirmed this linearity. These results can be explained by suggesting the predominant breakdown mechanism is thermionic emission. However, other breakdown mechanisms have also been investigated by TCAD simulations.

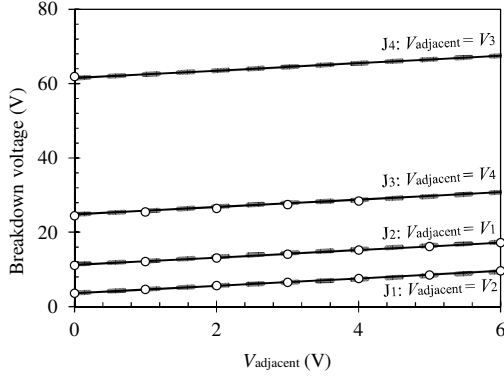


Fig. 13: Breakdown voltage of the BQJ junctions as a function of their adjacent junction's voltage bias, obtained by the proposed model (thick lines), by TCAD simulations (dashed lines) and by measurements (dots).

Firstly, the BTB tunneling effect in a single pn junction has been studied by TCAD simulations using Hurkx model [20], with the aims of calibrating model parameters. Fig. 14a shows simulated I-V characteristic for an asymmetric junction with $N_D = 10^{20} \text{ cm}^{-3}$ and $N_A = 10^{18}, 10^{17}$ and 10^{16} cm^{-3} , respectively. Measured results of a pn junction from [21] for $N_D = 10^{20} \text{ cm}^{-3}$ and $N_A = 10^{18} \text{ cm}^{-3}$ are also plotted for comparison. With the agreement between simulated and measured data, we have maintained the same parameter values of the BTB tunneling model for simulating the BMJ structure.

Secondly, avalanche effect has been considered by using van Overstraeten-de Man model [22] integrated in TCAD software. The parameters have also been calibrated by comparing simulated results with measured data [23], as shown in Fig. 14b. Similarly, after observed agreement, the same parameter values have been used for simulating the BMJ structure.

Finally, we have simulated the BQJ detector to obtain I-V curves with and without activating BTB and avalanche models. Fig. 15 draws the obtained results for the four junctions, showing no difference of results between activation and deactivation of the two models. These results preclude BTB and avalanche effects as responsible for the observed breakdown in the BQJ detector, and thus confirm that the thermionic emission is the predominant mechanism.

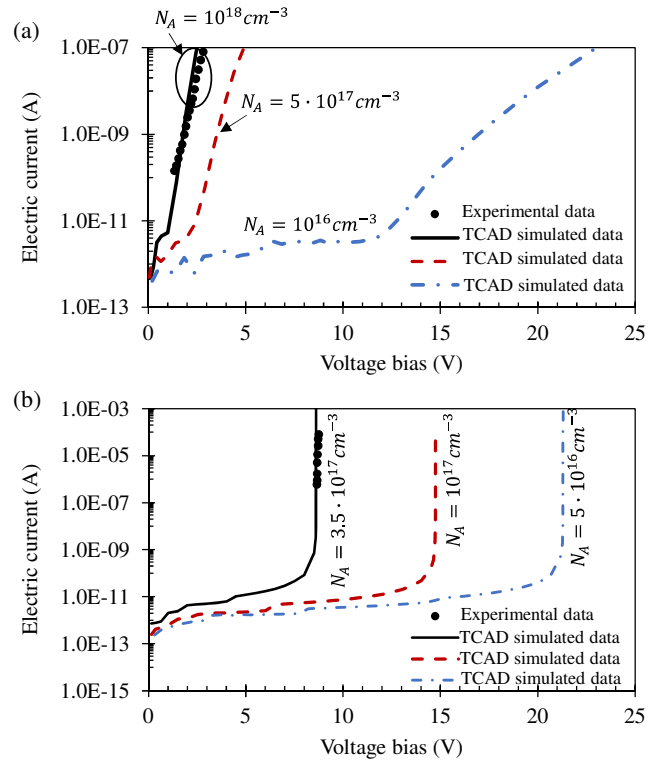


Fig. 14: TCAD simulations of a single asymmetric pn junction, after calibration of model parameters by comparison with measured data. (a) Breakdown due to BTB tunneling effect (using Hurkx model) for the junction with doping concentrations: $N_D = 10^{20} \text{ cm}^{-3}$ and $N_A = 10^{18}, 10^{17}$ and 10^{16} cm^{-3} . The measured data are from [21]. (b) Avalanche-caused breakdown (using van Overstraeten-de Man model) for the junction with doping concentrations: $N_D = 9.5 \cdot 10^{18} \text{ cm}^{-3}$ and $N_A = 3.5 \cdot 10^{17}, 10^{17}$ and $5 \cdot 10^{16} \text{ cm}^{-3}$. The measured data are from [23].

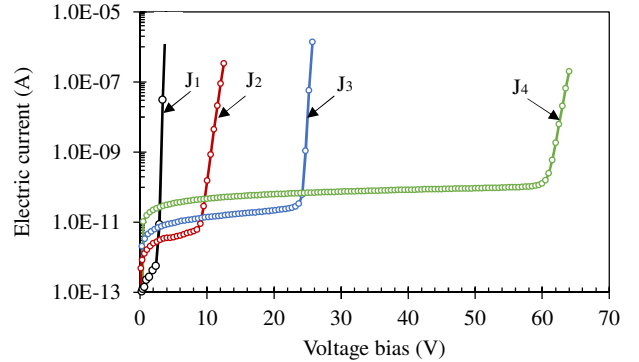


Fig. 15: TCAD-simulated I-V characteristics of the BQJ detector, with (lines) and without (dots) activation of BTB and avalanche models, respectively.

IV. CONCLUSIONS

We have established an analytical model to describe voltage breakdown shift behavior of the BMJ detector. It determines the merged depletion region limits between two adjacent junctions, electric field and electrostatic potential profile. Then, the potential barrier height is extracted and the thermionic current across the barrier is calculated. The model computations have been compared with TCAD simulations and measurements on different structures in different bias conditions at different temperatures. The observed agreement is a validation of the proposed model. BTB and avalanche effects have also been investigated by TCAD simulations.

They are not responsible for the observed breakdown shift in the BMJ detector. This model is an alternative to finite elements based approaches such as TCAD: it requires less intensive computations and is less sensitive to convergence issues.

ACKNOWLEDGEMENTS

This research did not receive any specific grant from funding agencies in the public, commercial, or not-for-profit sectors.

REFERENCES

- [1] G. N. Lu, M. B. Chouikha, G. Sou, and M. Sedjil, "Colour detection using a buried double p-n junction structure implemented in the CMOS process," *Electron. Lett.*, vol. 32, no. 6, p. 594, 1996.
- [2] S. Schidl, A. Polzer, J. Dong, and H. Zimmermann, "Investigation of transient photocurrent response of triple pn junction structure," *Electron. Lett.*, vol. 49, no. 4, pp. 4–6, 2013.
- [3] S. Schidl, R. Enne, and H. Zimmermann, "Blue enhanced vertically stacked quad junction photodetector with opto window," *Electron. Lett.*, vol. 51, no. 10, pp. 777–778, 2015.
- [4] C. Richard *et al.*, "CMOS buried quad p-n junction photodetector for multi-wavelength analysis.," *Opt. Express*, vol. 20, no. 3, pp. 2053–61, 2012.
- [5] A. Rush and P. Hubel, "X3 Sensor Characteristics," *J. Soc. Photogr. Sci. Technol. Japan.*, vol. 66, no. 1, pp. 57–60, 2003.
- [6] T. Courcier *et al.*, "CMOS BQJ detector chip with integrated charge-amplifiers for fluorescence measurements," *Sensors Actuators, B Chem.*, vol. 190, pp. 288–294, 2014.
- [7] A. Von Chong, M. Terosiet, A. Histace, and O. Romain, "Towards a novel single-LED pulse oximeter based on a multispectral sensor for IoT applications," *Microelectronics J.*, 2018.
- [8] Z. Zhan *et al.*, "Filterless optical oxygen sensor based on a CMOS buried double junction photodiode," *Sensors Actuators B. Chem.*, vol. 176, pp. 729–735, 2013.
- [9] S. Feruglio *et al.*, "Opto-Electrical Modeling of CMOS Buried Quad Junction Photodetector," *Key Eng. Mater.*, vol. 605, pp. 470–473, 2014.
- [10] T. L. V. N. Silva, G. N. Lu, and P. Pittet, "Breakdown Voltage Shift of CMOS Buried Quad Junction (BQJ) Detector," in *XXXIII Conference on Design of Circuits and Integrated Systems*, 2018, pp. 1–6.
- [11] J. Lohstroh, J. J. M. Koomen, A. T. Van Zanten, and R. H. W. Salters, "Punch-through currents in P+NP+ and N+PN+ sandwich structures—II: General low-injection theory and measurements," *Solid. State. Electron.*, vol. 24, no. 9, pp. 815–820, Sep. 1981.
- [12] J. Lohstroh, J. J. M. Koomen, A. T. Van Zanten, and R. H. W. Salters, "Punch-through currents in P+NP+ and N+PN+ sandwich structures—I: Introduction and basic calculations," *Solid. State. Electron.*, vol. 24, no. 9, pp. 805–814, Sep. 1981.
- [13] K. K. N. S.M.Sze, *Physics of Semiconductor Devices Physics of Semiconductor Devices*, vol. 10. Wiley-Interscience, 1995.
- [14] D. Jäger, P. Paulus, and R. Heidemann, "The BARITT diode — A low noise heterodyne photodetector with high integral gain," *Phys. B+C*, vol. 129, no. 1, pp. 501–505, 1985.
- [15] R. van Dalen, G. E. J. Koops, and O. Pfennigstorf, "Punch-through diodes as replacement for low-voltage Zener diodes in ESD protection circuits," *J. Electrostat.*, vol. 61, no. 3–4, pp. 149–169, Jul. 2004.
- [16] S. Esener and S. H. Lee, "Punchthrough current under diffusionlimited injection: Analysis and applications," *J. Appl. Phys.*, vol. 58, no. 3, pp. 1380–1387, 1985.
- [17] P. Papadopoulou, N. Georgoulas, L. Georgopoulos, and A. Thanailakis, "A model for the dc electrical behavior of bulk-barrier diodes," *Electr. Eng.*, vol. 83, no. 4, pp. 203–211, 2001.
- [18] J. L. Chu, G. Persky, and S. M. Sze, "Thermionic injection and space-charge-limited current in reach-through p+np+structures," *J. Appl. Phys.*, vol. 43, no. 8, pp. 3510–3515, 1972.
- [19] N. Rouger, "Electric field distribution and voltage breakdown modeling for any PN junction," *COMPEL Int. J. Comput. Math. Electr. Electron. Eng.*, vol. 35, no. 1, pp. 137–156, 2016.
- [20] G. A. M. Hurkx, D. B. M. Klaassen, and M. P. G. Knuvers, "New Recombination Model for Device Simulation Including Tunneling," *IEEE Trans. Electron Devices*, vol. 39, no. 2, pp. 331–338, 1992.
- [21] J. Yipeng, W. Kangliang, W. Taihuan, D. Gang, and L. Xiaoyan, "Comparison of band-to-band tunneling models in Si and Si — Ge junctions," *J. Semicond.*, vol. 34, no. 09, pp. 1–5, 2013.
- [22] H. D. Man and R. V. Overstraeten, "Measurement of the Ionization Rates in Diffused Silicon P-N Junctions," *Solid State Electron.*, vol. 13, no. 1, pp. 583–608, 1970.
- [23] M. M. Hossain, P. Zarkesh-Ha, and M. M. Hayat, "Linear mode CMOS compatible p-n junction avalanche photodiode with operating voltage below 9V," *2015 IEEE Photonics Conf. IPC 2015*, vol. 1, pp. 436–437, 2015.